

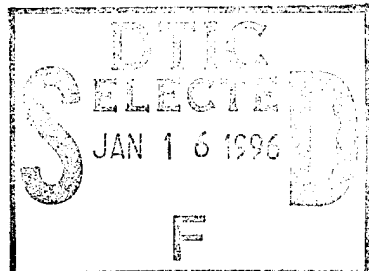
# NATIONAL AIR INTELLIGENCE CENTER



THEORY AND NUMERICAL VALUE CALCULATIONS ASSOCIATED WITH  
STIMULATED RAMAN SCATTERING IN THE ATMOSPHERE

by

Lin Dewen



Approved for public release:  
distribution unlimited

19960104 014 —

DIGITAL QUALITY INSPECTED 1

**HUMAN TRANSLATION**

NAIC-ID(RS)T-0509-95      6 December 1995

MICROFICHE NR: 95C000759THEORY AND NUMERICAL VALUE CALCULATIONS ASSOCIATED WITH  
STIMULATED RAMAN SCATTERING IN THE ATMOSPHERE(Selected Articles)

By: Lin Dewen

English pages: 36

Source: Qiangjiguang Yu Zizishu (High Power Laser and  
Particle Beams), Vol. 6, Nr. 2, May 1994;  
pp. 1; 193-200; 215-220; 297-302

Country of origin: China

Translated by: SCITRAN

F33657-84-D-0165

Requester: NAIC/TATD/Bruce Armstrong

Approved for public release: distribution unlimited.

THIS TRANSLATION IS A RENDITION OF THE ORIGINAL FOREIGN TEXT WITHOUT ANY ANALYTICAL OR EDITORIAL COMMENT STATEMENTS OR THEORIES ADVOCATED OR IMPLIED ARE THOSE OF THE SOURCE AND DO NOT NECESSARILY REFLECT THE POSITION OR OPINION OF THE NATIONAL AIR INTELLIGENCE CENTER.	PREPARED BY:
	TRANSLATION SERVICES NATIONAL AIR INTELLIGENCE CENTER WPAFB, OHIO

PREPARED BY:

TRANSLATION SERVICES  
NATIONAL AIR INTELLIGENCE CENTER  
WPAFB, OHIO

#### **GRAPHICS DISCLAIMER**

**All figures, graphics, tables, equations, etc. merged into this translation were extracted from the best quality copy available.**

Action For	
NTIS	GRACI
DTIC	TAB
Unclassified	
Justification	
By	
Distribution /	
Availability Codes	
Dist	Aval and/or Special
A-1	

**ABSTRACT** Starting out from the basic principles of quantum mechanics, the dynamics equations for stimulated Raman scattering (SRS) under semi-classical theoretical conditions are obtained. Theoretical verification is done of the fact that classical descriptions are only appropriate provided the distance between upper and lower energy levels is relatively great. Numerical simulations are done of several types of effects associated with stimulated rotational Raman scattering (SRRS) when strong lasers pass through the atmosphere. In these are included influences associated with Raman rotational properties, SRRS threshold values, and molecular "memory" on pulse series transmission.

**KEY WORDS** Stimulated rotational Raman scattering Semi-classical theory Transforming threshold Pulse series

## I INTRODUCTION

In research on stimulated Raman scattering, particle systems are normally described by the use of classical resonance sub-equations [1]

$$\frac{\partial Q^*}{\partial t} + \Gamma Q^* = \frac{i\alpha'}{4\omega_s M} \tilde{E}_L \tilde{E}, \quad (1)$$

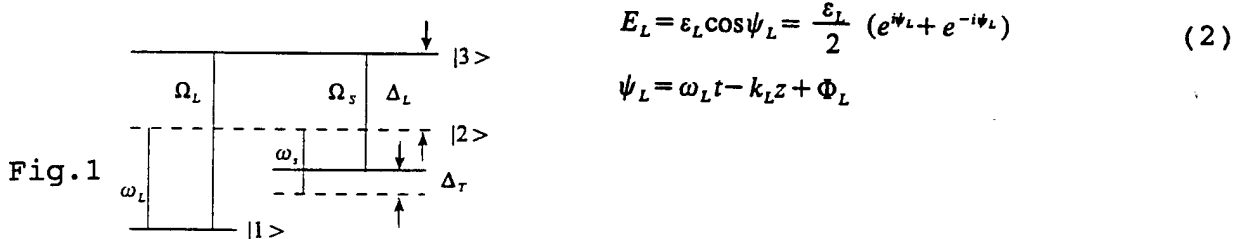
As far as stimulated vibratory Raman scattering (SVRS), which occurs in molecules under outside field effects, is concerned, opting for the use of classical descriptions discussed above can be understood. It has already been clearly demonstrated that, when strong laser light passes through the atmosphere, SRRS is primarily involved. With respect to this type of molecular transition between rotation states, there is no corresponding classical model. There are also problems awaiting investigation as to whether or not it is possible to make use of classical resonance sub-equation (1) to apply descriptions. From the fundamental principles of quantum mechanics  $\partial\hat{\rho}/\partial t = -i[\hat{H}, \hat{\rho}]/\hbar$  and  $p = Tr(\hat{\rho}\hat{\mu})$ , this article sets out to solve particle field Bloch equations and field polarization p. Moreover, fields themselves still obey classical wave equations.

## 2 DYNAMICS EQUATION SETS ASSOCIATED WITH SEMI-CLASSICAL THEORIES OF

### STIMULATED RAMAN SCATTERING

#### 2.1 Particle System Bloch Equations

Assume that particle systems possess the three energy levels shown in Fig.1. As far as lasers in TEMoo are concerned,



$$E_L = \epsilon_L \cos \psi_L = \frac{\epsilon_L}{2} (e^{i\psi_L} + e^{-i\psi_L}) \quad (2)$$

$$\psi_L = \omega_L t - k_L z + \Phi_L$$

Under these effects, Raman scattering will occur. The scattered light is

$$E_s = \varepsilon_s \cos \psi_s = \frac{\varepsilon_s}{2} (e^{i\psi_s} + e^{-i\psi_s}) \quad (3)$$

$$\psi_s = \omega_s t - k_s z + \Phi_s$$

/194

(Illegible) system Hamilton quantities are

$$\hat{H} = \hat{H}_0 + \hat{H}_1$$

$$\hat{H}_0 = \begin{bmatrix} \hbar\omega_1 & 0 & 0 \\ 0 & \hbar\omega_2 & 0 \\ 0 & 0 & \hbar\omega_3 \end{bmatrix} \quad \hat{H}_1 = \begin{bmatrix} 0 & 0 & V_L \\ 0 & 0 & V_S \\ V_L & V_S & 0 \end{bmatrix}$$

Dipole transition  $V_x = -\mu_x E_x$ , ( $\alpha = L, S$ ), Dipole transition matrix elements  $\mu_L = -\langle 1|qr|3\rangle, \mu_S = -\langle 2|qr|3\rangle$ .

The atmosphere is primarily composed of dual homonuclear molecules such as N<sub>2</sub>, O<sub>2</sub>, H<sub>2</sub>, and so on. Dual homonuclear molecules, in and of themselves, have no permanent dipole moments. Transitions associated with molecular vibrating electrons still maintaining base states invariably do not produce induction dipole moments either. As far as the production of dipole moments is concerned, it is necessary that they be accompanied by stimulated electron states--under the effects of electric field incidence, electron charge distributions give rise to relative shifts. This is nothing else than to say that |3> states belong to the class of excited electron states. With regard to SRRS, |1> states and |2> states should belong to two rotation states in the same vibratory state.

By solving equation  $\partial\hat{\rho}/\partial t \equiv \dot{\hat{\rho}} = -i[\hat{H}, \hat{\rho}]/\hbar$  satisfying density calculations  $\hat{\rho} = |\psi\rangle\langle\psi|$

$$\dot{\rho}_{12} = -i\omega_{12}\rho_{12} + i[d_L\varepsilon_L\rho_{32}(e^{i\psi_L} + e^{-i\psi_L}) - d_S^*\varepsilon_S\rho_{13}(e^{i\psi_S} + e^{-i\psi_S})] \quad (4)$$

$$\dot{\rho}_{22} - \dot{\rho}_{11} = i[\varepsilon_S(d_S\rho_{23}^* - d_S^*\rho_{23})(e^{i\psi_S} + e^{-i\psi_S}) - \varepsilon_L(d_L\rho_{13}^* - d_L^*\rho_{13})(e^{i\psi_L} + e^{-i\psi_L})] \quad (5)$$

$$\dot{\rho}_{33} = i[(d_L^*\varepsilon_L\rho_{13} - d_L\varepsilon_L\rho_{13}^*)(e^{i\psi_L} + e^{-i\psi_L}) + (d_S^*\varepsilon_S\rho_{23} - d_S\varepsilon_S\rho_{23}^*)(e^{i\psi_S} + e^{-i\psi_S})] \quad (6)$$

In this,  $d_z = \mu_z/2\hbar$ , ( $\alpha = L, S$ ). Use  $\delta_i$  to stand for normal  $\delta_i$  phases. Moreover, note  $\delta_L = \delta_3 - \delta_1 = \delta_{13}$ ,  $\delta_S = \delta_3 - \delta_2 = \delta_{23}$ , and  $\delta\lambda = \delta_2 - \delta_1 = \delta_{12}$ .

From similar equations associated with  $\dot{\rho}_{13}, \dot{\rho}_{23}$ , solutions are done for |13 and |23 (approximate solutions). Again, substituting into equations (4), (5), and (6), high frequency terms are eliminated, and one obtains [2]

$$\dot{\sigma}_{12} = i\{(\Omega_\lambda + \beta\Omega_{Sf})\sigma_{12} + \Omega_e(\rho_{22} - \rho_{11})(e^{i\psi_L} + (\beta - 1)e^{-i\psi_L})\} \quad (7)$$

$$\dot{\rho}_{22} - \dot{\rho}_{11} = i[\tilde{d}_S\varepsilon_S(e^{i\psi_S} + e^{-i\psi_S})(\sigma_{23}^* - \sigma_{23}) - \tilde{d}_L\varepsilon_L(e^{i\psi_L} + e^{-i\psi_L})(\sigma_{13}^* - \sigma_{13})] \quad (8)$$

$$\dot{\rho}_{33} = 0$$

(9)

Here are introduced the signs  $d_\alpha = \tilde{d}_\alpha e^{i\delta_\alpha}$  ( $\alpha = L, S, \lambda$ ),  $\sigma_{nm} = \rho_{nm} e^{i\delta_{nm}}$ ,  $\Omega_\lambda = \Omega_{21} = -\omega_{12}$ ,  $\Omega_\epsilon = 2\tilde{d}_L \tilde{d}_S \epsilon_L \epsilon_S / \Delta_L$ ,  $\Omega_{sj} = (\tilde{d}_L^2 \epsilon_L^2 - \tilde{d}_S^2 \epsilon_S^2) / \Delta_L$ .  $\beta = \beta(\omega_S / \Delta_L)$  called drift frequencies).

$= 1 + \frac{1}{1 + (2\omega_S / \Delta_L)}$ ,  $\psi_\lambda = (\omega_L - \omega_S)t - (k_L - k_S)z + (\Phi_L - \Phi_S) = \omega_\lambda t - \Delta kz + \Delta\Phi$ .  
Let  $\dot{R}_1 = \sigma_{12} + \dot{\sigma}_{12}$ ,  $R_2 = -i(\sigma_{12} - \dot{\sigma}_{12})$ ,  $R_3 = \rho_{22} - \rho_{11}$ ;  $\omega_1 = -\beta\Omega_\epsilon \cos\psi_\lambda$ ,  $\omega_2 = (\beta - 2)\Omega_\epsilon \sin\psi_\lambda$ ,  $\omega_3 = \Omega_\lambda + \beta\Omega_{sj}$ ,

Using (R1, R2, R3) to be the three components constituting vector R, and using (R1, R2, R3) to be the three components constituting vector  $\dot{\omega}$ , one then has

$$\dot{R} = \dot{\omega} \times R \quad (10)$$

That is, during stimulated Raman scattering, particle systems satisfy Bloch equations. Normally,  $\Omega_\epsilon \ll \Omega_\lambda$ . R is primarily rotational around 3 axes.

Doing transforms

$$\begin{bmatrix} R_1 \\ R_2 \\ R_3 \end{bmatrix} = \begin{bmatrix} \cos\psi_\lambda & -\sin\psi_\lambda & 0 \\ \sin\psi_\lambda & \cos\psi_\lambda & 0 \\ 0 & 0 & 1 \end{bmatrix} \begin{bmatrix} u_\lambda \\ v_\lambda \\ w_\lambda \end{bmatrix}$$

/195 Leaving out high frequency terms, one obtains

(11) The three components of vector  $R_\lambda$  are  $(u_\lambda, v_\lambda, w_\lambda)$ .  
The three components of the vector  $\dot{R}_1$  are  $(-\Omega_\epsilon, 0, \beta\Omega_{sj} - \Delta\Phi)$ .  
The rate of time change associated with Rlambda will be much slower than R.

This article adopts  $\beta = 1$ . At this time, it is equivalent to adopting  $E_\alpha = \frac{1}{2} \epsilon_\alpha e^{i\psi_\alpha}$ , ( $\alpha = L, S$ ). This is nothing else

than saying that rotational wave approximations in resonance optics are also appropriate for use with regard to SRRS processes.

Taking stimulated particle attenuations and phenomenologically introducing them into motion equations, one has

$$\dot{u}_\lambda = -(\Delta_\epsilon - \Delta\Phi)v_\lambda - \Gamma u_\lambda \quad (12)$$

$$\dot{v}_z = (\Delta_\epsilon - \Delta\Phi) u_z + \Omega_\epsilon w_z - \Gamma v_z \quad (13)$$

$$\dot{w}_z = -\Omega_\epsilon v_z - \Gamma_1 (w_z - w_\epsilon) \quad (14)$$

In these,  $1/\Gamma_1 = t_1$  is longitudinal relaxation times.  $1/\Gamma = t_2$  is transverse relaxation times.  $w_\epsilon$  is an equilibrium value for particle number reversal when there is no field.  $W_e = \Omega_{sf} + \Delta T$ .  $\Delta T$  is Fig.1's detuning amount [3].

## 2.2 Field Equations

Electric field  $E_\alpha$  ( $\alpha = L, S$ ) satisfies wave equation

$$(\frac{\partial^2}{\partial t^2} - \frac{1}{c^2} \frac{\partial^2}{\partial z^2}) E_\alpha = \frac{4\pi N_0}{c_0^2} \frac{\partial^2 p_\alpha}{\partial z^2} \quad (15)$$

$N_0$  is particle number density.  $p = \Sigma p_\alpha$  is a particle polarization.  $N_0 p$  is macropolarization strength.  $c = c_0/n$  is the speed of light in media.  $n$  is index of refraction (Here, chromatic dispersion is ignored).  $c_0$  is the speed of light in a vacuum.

According to the basic principles of quantum mechanics, 5  
 $p = Tr(\hat{p}\hat{\mu})$ . Solving, one gets

$$p_L = \tilde{\mu}_L (\sigma_{13} + \sigma_{13}^\dagger)$$

$$p_S = \tilde{\mu}_S (\sigma_{23} + \sigma_{23}^\dagger)$$

In this,  $\tilde{\mu}_z = |\mu_z| = 2\hbar d_z$ , that is,  $\mu_z = \tilde{\mu}_z e^{i\delta_z}$ .

Taking polarization and dividing it into two parts--isophase and nonisophase

(16)

Let  $R_{z1} = \sigma_z + \sigma_z^\dagger$ ,  $R_{z2} = -i(\sigma_z - \sigma_z^\dagger)$ . In this

$$\sigma_z = \begin{cases} \sigma_{13} & , \text{ 当 } \alpha = L \text{ 时} \\ \sigma_{23} & , \text{ 当 } \alpha = S \text{ 时} \end{cases}$$

Between  $(R_{z1}, R_{z2})$  and  $(u_z, v_z)$ , the transforms below are satisfied

$$\begin{bmatrix} R_{z1} \\ R_{z2} \end{bmatrix} = \begin{bmatrix} \cos\psi_\alpha & -\sin\psi_\alpha \\ \sin\psi_\alpha & \cos\psi_\alpha \end{bmatrix} \begin{bmatrix} u_\alpha \\ v_\alpha \end{bmatrix}$$

Making use of  $\sigma_{13}$  and  $\sigma_{23}$  as already solved for, one obtains

$$(17) \quad u_L = \frac{1}{\Delta_L} [\tilde{d}_s \varepsilon_s u_\lambda - 2\tilde{d}_L \varepsilon_L (\rho_{33} - \rho_{11})]$$

/196

$$(18) \quad v_L = \frac{1}{\Delta_L} \tilde{d}_s \varepsilon_s v_\lambda$$

$$(19) \quad u_s = \frac{1}{\Delta_L} [\tilde{d}_L \varepsilon_L u_\lambda - 2\tilde{d}_s \varepsilon_s (\rho_{33} - \rho_{22})]$$

$$(20) \quad v_s = \frac{1}{\Delta_L} \tilde{d}_L \varepsilon_L v_\lambda$$

Particle number conservation requires  $\rho_{33} + \rho_{22} + \rho_{11} = 1$ . From equation (9), one obtains  $\rho_{33} = C_1$ . Therefore,  $\rho_{22} + \rho_{11} = C_2$ .  $C_1$  and  $C_2$  are constants. It is possible to see that, during stimulated Raman scattering processes, transitions only arise between state  $\rho_{1>}$  and state  $\rho_{2>}$ . The arrangement of state  $\rho_{3>}$  particles is maintained invariable throughout.  $\rho_{3>}$  is designated as intermediate state.  $C_1$  and  $C_2$  are determined by initial conditions.

It has been pointed out before that, with regard to dipole transitions,  $\rho_{3>}$  is an electron excitation state. The energy difference between it and a base state is approximately 10eV. Therefore,  $C_1 = 0$ .  $C_2 = 1$ . Because of this, one solves to get

$$\rho_{33} - \rho_{22} = -\frac{1}{2} (w_\lambda + 1) \quad (21)$$

$$\rho_{33} - \rho_{11} = \frac{1}{2} (w_\lambda - 1) \quad (22)$$

Taking equations (17)-(22) and substituting into equation (16), one gets

$$p_L = \tilde{\mu}_L \left\{ \frac{1}{\Delta_L} [\tilde{d}_s \varepsilon_s u_\lambda - \tilde{d}_L \varepsilon_L (w_\lambda - 1)] \cos \psi_\lambda - \frac{1}{\Delta_L} \tilde{d}_s \varepsilon_s v_\lambda \sin \psi_L \right\} \quad (23)$$

$$p_s = \tilde{\mu}_L \left\{ \frac{1}{\Delta_L} [\tilde{d}_L \varepsilon_L u_\lambda + \tilde{d}_s \varepsilon_s (w_L + 1)] \cos \psi_L + \frac{1}{\Delta_L} \tilde{d}_L \varepsilon_L v_\lambda \sin \psi_s \right\} \quad (24)$$

$$\frac{\partial^2 p_a}{\partial t^2} = -(\omega_a + \dot{\Phi}_a)^2 p_a \approx -\omega_a^2 p_a \quad (25)$$

Taking equations (23)-(25) and substituting into equation (15), comparisons of  $\cos \psi_a$  and  $\sin \psi_a$  coefficients arrive at equations associated with slow change amplitudes  $\varepsilon_a$  and slow change phases  $\Phi_a$  of fields (consider  $\omega_a \gg \dot{\Phi}_a$ ,  $k_a \gg \frac{\partial \Phi_a}{\partial z}$ )

$$\left( \frac{\partial}{\partial z} + \frac{1}{c} \frac{\partial}{\partial t} \right) \varepsilon_L = \beta_L \varepsilon_s v_\lambda \quad (26)$$

$$\left( \frac{\partial}{\partial z} + \frac{1}{c} \frac{\partial}{\partial t} \right) \Phi_L = -\beta_L \left[ \frac{\varepsilon_s}{\varepsilon_L} u_\lambda - \frac{\tilde{\mu}_L}{\tilde{\mu}_s} (w_\lambda - 1) \right] \quad (27)$$

$$\left( \frac{\partial}{\partial z} + \frac{1}{c} \frac{\partial}{\partial t} \right) \varepsilon_s = -\beta_s \varepsilon_L v_\lambda \quad (28)$$

$$\left( \frac{\partial}{\partial z} + \frac{1}{c} \frac{\partial}{\partial t} \right) \Phi_s = -\beta_s \left[ \frac{\varepsilon_L}{\varepsilon_s} + \frac{\tilde{\mu}_s}{\tilde{\mu}_L} (w_\lambda + 1) \right] \quad (29)$$

In this,

$$\beta_\alpha = \frac{\pi N_0 \omega_s \tilde{\mu}_L \tilde{\mu}_s}{c_0^2 \hbar \Delta_L}, \quad (\alpha = L, S)$$

### 3 CLASSICAL STIMULATED RAMAN SCATTERING DESCRIPTIONS AS WELL AS THE APPROPRIATE CONDITIONS FOR USE

Let

$$\text{令 } \tilde{E}_\alpha = \varepsilon_\alpha e^{i\Phi_\alpha} \quad (30)$$

/197

$$Q = (u_\lambda + iv_\lambda) e^{i\Delta\Phi} \quad (\Delta\Phi = \Phi_L - \Phi_s) \quad (31)$$

If one adopts  $w_\lambda = w_e$  ( $\dot{w}_\lambda = 0$ ), then the fixed solution equation set becomes

$$\left( \frac{\partial}{\partial z} + \frac{1}{c} \frac{\partial}{\partial t} \right) \tilde{E}_L = -i\beta_L \left[ \tilde{E}_s Q - \frac{\tilde{\mu}_L}{\tilde{\mu}_s} (w_e - 1) \tilde{E}_L \right] \quad (32)$$

$$\left( \frac{\partial}{\partial z} + \frac{1}{c} \frac{\partial}{\partial t} \right) \tilde{E}_s = -i\beta_s \left[ \tilde{E}_L Q + \frac{\tilde{\mu}_s}{\tilde{\mu}_L} (w_e + 1) \tilde{E}_s \right] \quad (33)$$

$$\left[ \frac{\partial}{\partial t} + (\Gamma + i\Delta_e) \right] Q^\bullet = -ik_1 w_e \tilde{E}_L \tilde{E}_s \quad (34)$$

In this,  $k_1 = \frac{\tilde{\mu}_L \tilde{\mu}_s}{2\hbar \Delta_L}$ . Normally, one has  $\Delta e \ll \Gamma$ . If  $w_e = -1$ , then equations (33) and (34) change to become

$$\left( \frac{\partial}{\partial z} + \frac{1}{c} \frac{\partial}{\partial t} \right) \tilde{E}_s = -ik_2 \tilde{E}_L Q^\bullet, \quad (k_2 = \beta_s) \quad (35)$$

$$\left( \frac{\partial}{\partial t} + \Gamma \right) Q^\bullet = ik_1 \tilde{E}_L E_s \quad (36)$$

When pump light  $\tilde{E}_L$  does not attenuate, equations (35) and (36) form a closed equation set. It is nothing else than molecular Raman scattering (Stokes wave and photon phonon wave) coupling equations.  $Q$  is simple positive molecular vibration coordinates, also designated as photon phonon waves. In reality, from equation (31), it is possible to see that  $Q$  reflects changes associated with particle systems  $(u_\lambda, v_\lambda)$ . At the same time, it also reflects changes in field phase  $(|\Phi|)$ . So long as field phase differences  $|\Phi$  are maintained constant,  $Q$  then, and

only then, belongs purely to particle "coordinates".

Key conditions for transitioning to classical descriptions are  $w_\lambda = w_e = -1$ , that is, particle lay out numbers associated with transition upper energy levels are zero ( $\rho_{22} = 0$ ). The ratio associated with first molecular vibration excitation states and base state lay outs are [4]  $\rho_{22} / \rho_{11} = 1.4 \times 10^{-5}$ . Therefore, classical descriptions are capable of giving good results with regard to molecular vibration Raman scattering. With regard to arrangement differences associated with two rotational energy levels on vibration base states, they are [5]  $w_e = -0.035$ . It is possible to see that classical equations will have relatively large errors with regard to describing SRRS. However, provided corrections are made to  $|N=N_0|w_e|$ , classical equations are still capable of giving good results.

#### 4 CALCULATION RESULTS

Fixed solution equations are simultaneous equation sets composed of 7 equations--(12)-(14) and (26)-(29).

##### 4.1 Parameter Determination

When material reaches a stable state ( $\dot{u}_\lambda = \dot{v}_\lambda = \dot{w}_\lambda = 0$ ), it is possible to solve and obtain

$$v_\lambda = \frac{\Omega_e w_e \Gamma}{\Gamma^2 + (\Gamma/\Gamma_1) \Omega_e^2 + (\Delta_e - \Delta \Phi)^2} \quad (37)$$

(Illegible) the equations above and substituting into equation (28), it is possible to obtain

$$\left( \frac{\partial}{\partial z} + \frac{1}{c} \frac{\partial}{\partial t} \right) I_s = \gamma I_L I_s$$

In this  $I_z = \frac{c_0 \delta_z^2}{4\pi}$ , ( $\alpha = L, S$ );

$$\gamma = \frac{\delta \pi^2 N_0 (-w_e) \Gamma}{c \hbar \lambda_s [\Gamma^2 + (\Gamma/\Gamma_1) \Omega_e^2 + (\Delta_e - \Delta \Phi)^2]} \approx \frac{8 \pi^2 N_0 (-w_e)}{c \Gamma \hbar \lambda_s} \left( \frac{\tilde{\mu}_L \tilde{\mu}_S}{\hbar \Delta_L} \right)^2$$

(Illegible) stable state gain coefficient. The setting up of the second equality in the equations above is because  $\Omega_e \ll \Gamma$  and  $(\Delta_e - \Delta \Phi) \ll \Gamma$ .  
Reference (5) gives

$$\gamma = \frac{64 \pi^3 N_0 (-w_e)}{15 \hbar M_S \Delta v_R c^2} \frac{(j+1)(j+2)}{(2j+1)(2j+3)} \gamma_{00}^2$$

Therefore,

$$\left( \frac{\tilde{\mu}_L \tilde{\mu}_S}{\hbar \Delta_L} \right)^2 = \frac{4}{15} \frac{(j+1)(j+2)}{(2j+1)(2j+3)} \gamma_{00}^2$$

$\Gamma = \Gamma_1$ ,  $\Delta_T = 0$ ,  $\lambda_L = 10^{-4}$

(photon phonon wave number). Adopting  $\tilde{\mu}_L = \tilde{\mu}_S$  cm<sup>-1</sup>,  $\lambda_S = \lambda_L - \lambda_{ph}$ ,  $\lambda_{ph}$  is photon phonon wave length. The values are solved for from photon phonon wave numbers  $v_{ph}$ .

Materials parameters are seen in Table 1 [5].

Table 1

Table 1 The parameters of materials

	$N_0(0)$ $/10^{19}\text{cm}^{-3}$	$\gamma_\infty$ $/10^{-24}\text{cm}^3$	$B$ $/\text{cm}^{-1}$	$w_e$	$\beta(j)/10^{-3}\cdot\text{ns}^{-1}$				
					6	8	10	12	14
$\text{N}_2$	2.237	0.693	2.001	-0.035	3560	3270	3060	2870	2660
$\text{O}_2$		1.099		1.4378	-0.039				

#### 4.2 Fixed Solution Conditions

Initial conditions: when  $t = 0$ ,  $u_\lambda(0) = v_\lambda(0) = 0$ ,  $w_\lambda(0) = w_e$ .

Boundary conditions: when  $t = 0$ , at ground locations ( $z = 0$ ), add a planar wave propagating along the  $z$  direction. These are Gaussian distributions following along with time changes. Wave lengths are  $|L|$ . Half widths are  $\tau$ . Peak value strengths are  $IL(0)$ . Seed illumination  $IS(0)$  is adopted as  $IS(0) = IL(0) \times 10^{-7}$ .

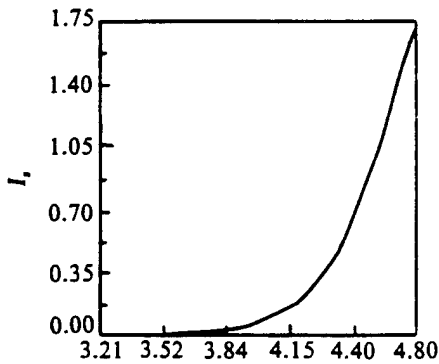
#### 4.3 Calculation Results

##### 4.3.1 SRRS Transformation Characteristics and Threshold Values

When strong lasers pass through the atmosphere, there is an intimate relationship between scattered light strengths  $IS$  associated with transformations and initial incident light strengths  $IL(0)$ . Concrete calculation results are as shown in Fig.2. When  $IL(0) > 3.9\text{MW/cm}^2$ , increases in  $IS$  following along with  $IL(0)$  are relatively slow. When  $IL(0) = 3.9\text{ MW/cm}^2$ ,  $IS$  increases rapidly following along with increases in  $IL(0)$ . When  $IL(0) = 3.9\text{ MW/cm}^2$ ,  $IS/IL(0) \approx 1\%$ . This pattern during strong laser atmospheric transmission possesses universality. The normal definition

$$\frac{I_s}{I_L(0)} = 1\%$$

Fig.2



$$I_s/\text{MW}\cdot\text{cm}^{-2}$$

Fig.2 Stokes intensity  $I_s$  as a function of the  
incident intensity  $I_L(0)$

of IL (0) is SRRS threshold value  $I_t$ . When  $IL(0) > I_t$ , emitted laser light IL will be scattered. Therefore, during research on strong laser light passing through the atmosphere, study of  $I_t$  for various types of wave lengths  $|L$  and pulse widths  $\tau$  is significant.

/199

Table 2 gives threshold values solved for different  $(\tau, |L|)$ .

Table 2

Table 2 Threshold of different  $(\tau, \lambda_L)$

$\tau/\text{ns}$	0.01	0.01	0.02	0.1	1.0	2.0	2.0
$\lambda_L/\mu\text{m}$	0.35	1.0	1.0	1.0	1.0	1.0	0.4
$I_t/\text{MW} \cdot \text{cm}^{-2}$	322	928	464	98.5	14.8	9.8	3.9

#### 4.3.2 Pulse Series Transmission Characteristics

Pulse series are composed of multiple pulses. The width of each pulse is  $\tau$ . The interval between various pulses is  $t$ . Therefore, what is different from single pulses about the transmission of pulse series is due to molecules possessing "memory" effects. Speaking in concrete terms, this is nothing else than a previous pulse later being forced by stimulated molecules into exponential attenuations as a function of time using  $e^{-\Gamma t}$  rules. See equations (12) and (13). In this way, with  $t < 1/\Gamma$ , when the second pulse arrives, the molecular stimulation which the first pulse creates is still partially retained. The second pulse is scattered by this type of stimulated molecule. If  $t \gg 1/\Gamma$ , obviously, pulse series are no different from the transmission of single pulses.

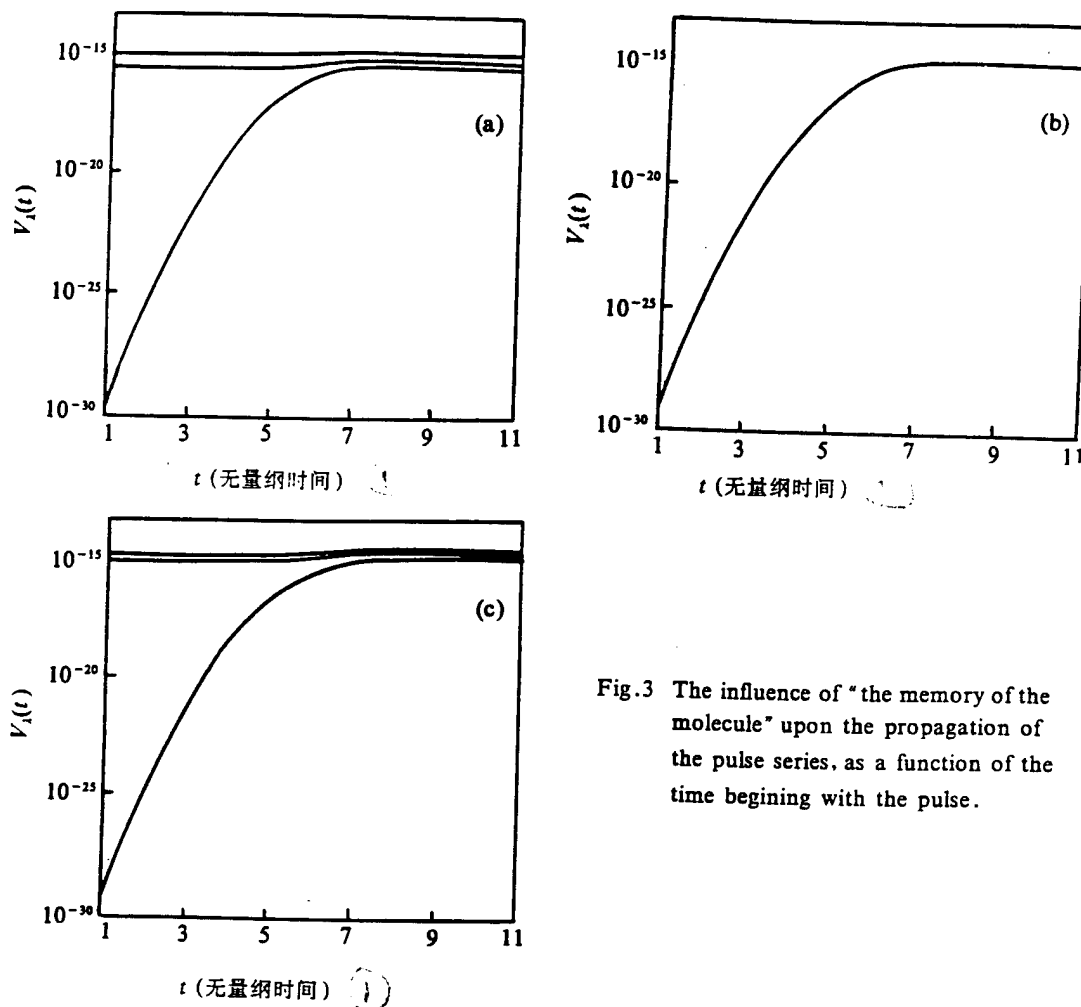


Fig.3 The influence of "the memory of the molecule" upon the propagation of the pulse series, as a function of the time beginning with the pulse.

Fig.3 The influence of "the memory of the molecule" upon the propagation of the pulse series, as a function of the time beginning with the pulse. (1) Dimensionless Time

What Fig.3 graphs out is curves ( $v_i$ ) associated with material stimulation created by pulse series pulses with serial numbers 1, 2, and 10.  $\tau$  is 0.02ns.  $IL(0) = 0.085\text{MW/cm}^2$ . Fig.3(a) is  $t = 2\text{ns}$ . This clearly shows that molecules have "memories". Stimulations are cumulative. Fig.3(b) is  $t = 20\text{ns}$ . The three lines converge together presenting single pulse characteristics.

Due to collision attenuation coefficient  $\Gamma \propto e^{-bt}$ , the higher the atmospheric level is, therefore, the stronger is molecular "memory", and the clearer accumulative effects are. Fig.3(b) is a case where the altitude is 10km. Fig.3(c) is a case where the altitude is 50km ( $t=20\text{ns}$ ). Molecules have "memories", and stimulations are cumulative.

## 5 ANALYSIS AND DISCUSSION

The driving term  $\Omega e$  associated with  $w_\lambda$  in equation (14) is normally very small. Therefore,  $w_\lambda$  deviation from equilibrium values we are very small. This is nothing else than the reason improved classical descriptions [6] give good results.

Due to the fact that the driving term  $\Omega e$  associated with  $v_\lambda$  in equation (12) is far larger than the driving term  $(\Delta_e - \Delta\Phi)v_\lambda$  associated with  $u_\lambda$  in equation (13), material polarization, therefore, is primarily characterized by nonisophasal component  $w_\lambda$ .

Seen from the view point of equations (26) - (28),  $v_\lambda$  directly influences changes in field amplitudes  $\varepsilon_\lambda$ . Then,  $u_\lambda$ , and  $\varepsilon_\lambda$  directly influence changes in field phases  $\Phi_\lambda$ . Field amplitudes  $\varepsilon_\lambda$  and field phases  $\Phi_\lambda$  do not directly give rise to coupling. By contrast, coupling is given rise to indirectly through materials systems.

When setting up computational plans, use is made of this type of coupling property to make program efficiencies relatively high. In 5 million operations a second computers, program cycles each only require 100  $\mu s$ .

## REFERENCES

- 1 Trutna WR, Park YK and Byer RL. *IEEE J Quantum Electron*, 1979, QE-15: 648 ~ 655
- 2 Naohiro Tan-no, Tsukasa Shirahata, and Kenichi Yokoto. *Phys. Rev*, 1975, A12 (1): 159 ~ 168
- 3 Raymer MG, Mostowski J, and Carlsten JL. *Phys Rev*, 1979, A19 (6): 2304 ~ 2316
- 4 赫兹堡 G. 分子结构与分子光谱. 中译本, 1983, 92
- 5 Rokni Mordechai and Flusberg Allen. *IEEE J Quantum Electron*, 1986, QE-22 (7): 1102 ~ 1108
- 6 Qri A and Rokni M. UCRL-15971. DE88 002470

MEASUREMENT OF ATMOSPHERIC COHERENCE LENGTH  
AND ISOPLANATIC ANGLE

Yang Gaochao Liu Xiaochun Fan Chengyu Song Zhengfang

Translation of "Da Qi Xiang Gan Chang Du Yu Deng Yun Jiao De Ce  
Liang"; HIGH POWER LASER AND PARTICLE BEAMS, Vol.6, No.2, May  
1994, pp 215-220

**ABSTRACT** This article introduces measurement principles associated with atmospheric coherence length and isoplanatic angle measuring instruments as well as the basic structures of instruments. It reports the results of measurements carried out at the Yunnan Observatory on Kunming's Phoenix Hill. The average value measured for  $r_0$  is 12.4cm. Average value for  $\theta_0$  is 10.6  $\mu$ rad. Compared to data associated with temperature pulsation probe instruments, the results obtained were demonstrated to be reliable. Finally, analyses were carried out with regard to a number of factors influencing measurement errors which can possibly exist in instruments.

**KEY WORDS** Atmospheric coherence length Isoplanatic angle  
Atmospheric seeing Adaptive optics

## I INTRODUCTION

In situations where use is made of adaptive optics systems, it is necessary to understand atmospheric seeing at the places and times concerned. The selection of sites for observatories and atmospheric seeing associated with daily astronomical observations are also one of the indispensable myriad parameters. Quantitative descriptions of atmospheric seeing parameters are nothing else than the so called Fried length [6] --- atmospheric coherence length  $r_0$ . This characterizes atmospheric coherence properties along certain transverse distances in a certain specially designated light path. In the same way, people are concerned with coherence characteristics between different light courses within certain ranges of distances or certain angles. This then requires making use of isoplanatic zones or isoplanatic angles in order to make descriptions. In actuality, what are made relatively more use of are isoplanatic angles, normally recorded as  $\Theta_0$ . In the middle 1980's, we began to make efforts in research work relating to atmospheric coherence [2]. In conjunction with this, an instrumentation unit to measure  $r_0$  and  $\Theta_0$  has been recently developed and manufactured successfully. This article is nothing else than the carrying out of a simple introduction to its measurement principles, instrument structure, and preliminary measurement results. Finally, analysis is done of error factors which can possibly exist.

## 2 MEASUREMENT PRINCIPLES

### 2.1 Atmospheric Coherence Length

The definition of atmospheric coherence length is

$$D(r) = 6.88 (r/r_0)^{5/3} \quad (\text{rad}^2) \quad (1)$$

That is, when receiving optical system radius  $r$  is equal to coherence length  $r_0$ , the value of wave structure function  $D(r)$  is 6.88 rad<sup>2</sup>. At this time, the properties of the systems in question reach optimum limits. Due to random propagation theory associated with waves in media, in air-ground light courses, planar waves  $r_0$ , are capable of being expressed as

$$r_0 = [0.422 k^2 \sec \psi \int_{h'}^{\infty} C_n^2(h) dh]^{-3/5} \quad (2)$$

In the equation,  $k=2\pi/\lambda$ .  $\lambda$  is wave length.  $\psi$  is the zenith angle.  $C_n^2(h)$  is height distributions associated with turbulent flow structure constants.  $h'$  is the altitude of measuring stations.

If it is possible to measure  $C_n^2(h)$ , it is then possible to calculate  $r_0$  from equation (2). Barletti and others [3] used this method to obtain height distributions associated with  $r_0$ .

The results were the same as  $\Gamma$  distribution models [4] we use/216

$$C_n^2(h) = C_0 h^{-2/3} \exp(-h/H_0) \quad (3)$$

Calculation results agree. In the equation,  $C_0$  and  $H_0$  are two set up parameters.  $H_0$  is analogous to the equivalent atmospheric altitude at the place and time in question.  $C_0$  corresponds to turbulence strengths associated with measurement station positions. However, normally, making use of this type of method in order to precisely determine  $r_0$  is very difficult. Moreover, it is also not possible to obtain results in real time. As a result, it is necessary to opt for the use of a type of indirect measurement method. In it, use is made of the earliest and most wide spread methods--which make use of arrival angles in order to do conversions. The theoretical expression associated with arrival angle fluctuation variances is

$$\sigma_a^2 = 2.905 D^{-1/3} \sec \psi \int_{h'}^{\infty} C_n^2(h) dh \quad (4)$$

In the equation,  $D$  is the diameter of the receiving telescope. From equation (2) and equation (4), it is possible to obtain

$$r_0 = 3.18 k^{-6/5} D^{-1/5} \sigma_a^{-6/5} \quad (5)$$

In early periods, measurements associated with arrival angles made use of photographic time exposure methods in order to record star fluctuations. From one dimensional directional time exposures, it is possible to obtain angular variance  $C_n^2$ . In order to make  $\sigma_{H_p}^2$  and  $\sigma_a^2$  equal to each other, an empirical constant exists between the two, that is,

$$\sigma_a^2 = b \sigma_{H_p}^2, \quad (6)$$

As far as adopted  $b$  values are concerned, there exists very great dispersion, making equation (6) become very imprecise. Besides this, due to such causes as data processing troubles, vibrations in instruments themselves, and so on, they can easily bring with them very great errors. Single light path arrival angle methods have gradually become known as "dual point difference arrival angle methods" or "difference imagery movement methods" [6] instead. This type of method takes light coming from a certain celestial body and, through certain measures, forms two celestial images on the receiving plane. Respective solutions are made for the differences  $\Delta p_{ci}$  of the two celestial images from their central position. Through the formula

$$r_0 = \left\{ \frac{2f^2 [0.36 (\lambda/D)^{1/2} - 0.242 (\lambda/d)^{1/3}] \lambda^{5/3}}{<\Delta p_{ci}^2> - <\Delta p_{ci}>^2} \right\}^{3/5} \quad (7)$$

$r_0$  is calculated. In the equation,  $f$  is telescope focal length.  $d$  is the central interval associated with the two light paths (that is also the theoretical interval associated with two images when there is no fluctuation). This type of method is not sensitive to such factors as perturbations in the instruments themselves, optical system quality, temperature effects on telescope focal length, fluctuations in star image brightness, and so on. As a result, it is possible to hope to obtain very good measurement precisions.

## 2.2 Isoplanatic Angles

The theoretical expression associated with isoplanatic angles is

$$\theta_0 = [2.905 k^2 \sec \psi \int_{h'}^{\infty} C_n^2(h) h^{5/3} dh]^{-3/5} \quad (8)$$

In the same way as  $r_0$ ,  $\theta_0$  daily observations must also go through observations of another physical quantity in order to carry out conversions. The most convenient solution is to use star light scintillation methods. This is due to the fact that the scintillation method  $\sigma^2$  also possesses altitude weighting functions similar to  $\theta_0$ . Theoretical calculations clearly show that, when  $D = 11\text{cm}$ , it is then possible to make the weighting functions associated with the two equal to each other [7]. In conjunction with this, the relationship set out below is established

$$\theta_0 = C [\log(1 + \sigma^2 / \langle S \rangle^2)]^{-3/5} \quad (9)$$

$\langle S \rangle$  is average values associated with star light signals.  $C$  is a constant. Through large amounts of experimentation, Eaton and others [8] indicate that  $C = 0.9676$ . Equation (9), during weak turbulence and medium strength turbulence, the precisions possessed are very good. It is only under strong turbulence conditions that errors can reach approximately 20%. In general cases, turbulence strengths throughout the entire atmosphere will not be in a strongly turbulent state. As a result, equation (9) is normally effective. /217

## 3 INSTRUMENT CONSTRUCTION

In our coherence length and isoplanatic angle measurement instruments, as far as measurements associated with  $r_0$  are concerned, use is made of dual point difference arrival angle methods. With regard to measurements associated with  $\theta_0$ , use is made of star light scintillation methods. The schematic diagram is as shown in Fig.1. Principal parameters are seen in Table 1. The instruments in question break down into two large parts--optical receiving systems and data processing systems. The former includes two receiving telescopes connected together with completely uniform properties, image merging light paths and two detectors (4720 model CCD pickup cameras and photoelectric

multiplier tubes). The entire system is installed on an equatorial type base. It is possible to use computers to control step electrical equipment to make searches and track in declination and right ascension directions. The latter includes video frequency cards, A/D cards, and 386 microcomputer systems.

Fig.1

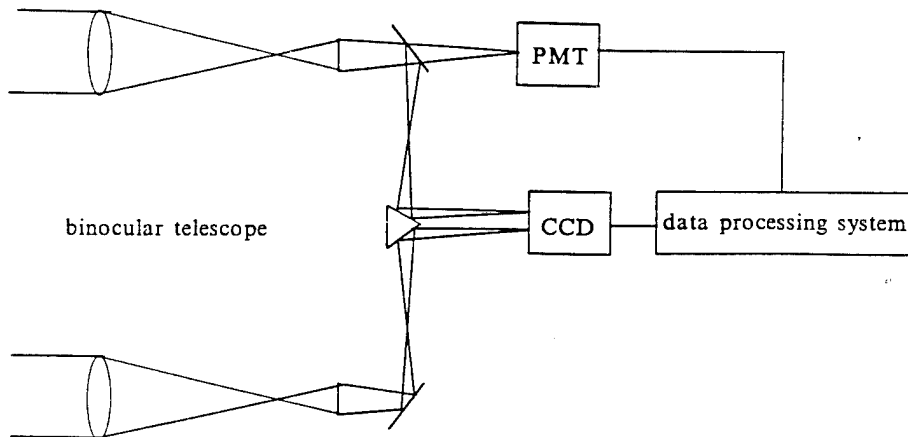


Fig.1 Schematic diagram of the  $r_0$  and  $\theta_0$  measurer

Table 1

Table 1 The main parameters of the  $r_0$  and  $\theta_0$  measurer

Optical system	Receiving aperture	$D/\text{cm}$	12
	Effective focal length	$f/\text{m}$	5
	Separation of centers	$d/\text{cm}$	15
	Visual angle of telescope	( $'$ )	3
	Visual angle of guiding telescope	( $''$ )	0.5
Image signal	Minimum illumination	$E_{\min}/\text{lX}$	0.02
	Signal-to-noise ratio	$SNR/\text{dB}$	52
	Sampling rate	$R/\text{Hz}$	25
	Sampling time	$t/\text{s}$	2.5
Intensity signal	Dark current	$I_0/\text{nA}$	50
	Sampling rate	$R/\text{Hz}$	1000
	Sampling time	$t/\text{s}$	5
Mechanical system	Type	Equatorial style	
	Right ascension	$\pm 100^\circ$	
	Declination	$\pm 45^\circ$	
	Tracking precision	$\leq 4''$	
	Weight	约200kg	

/218

The height of the entire instrument is approximately 1.2m. The length is approximately 1.6m. Right ascension and declination coordinates are picked up from 21 place photoelectric coding disks. At the same time as numeric tubes display right ascension and declination coordinate values, they are transferred to microcomputer to be recorded in order to act as a basis during normalized data processing.

CCD pick up cameras possess characteristics of low illumination and high signal to noise ratios. In order to be advantageous to the reception of celestial images with relatively weak optical powers, the signals go through video frequency collection cards, and are, first of all, entered into internal computer storage. The collection rate is 25 frames/s. Each iteration of observations is 2.5 s. After that, solutions are done for the two central positions  $\rho_{1i}$  and  $\rho_{2i}$ , thereby obtaining  $\Delta\rho_{ci} = \rho_{2i} - \rho_{1i}$ . Finally,  $r_0$  is calculated from equation (7).

When measuring  $\theta_0$ , computer processing inputs celestial image strength signals by A/D cards. Collection speed is 1kHz. The sampling period for each set of data is 5s. Reckoning up

signal fluctuation variance  $\sigma^2$  and average value  $\langle S \rangle$ , by using formula (9), it is then possible to calculate  $\Theta_0$ .

In order to resolve such problems as inadequate computer internal storage capacity and excessively long calculation times, when processing celestial image signals, option is made for the use of "window" methods. The size of windows must pay attention to all of imagery fluctuation ranges, mechanical adjustment precisions, and observation times. Considering imagery fluctuations, they are generally not larger than 2". Mechanical precisions are approximately 4". As a result, window height should not be less than 10". This corresponds to the 64 lines of a 512x512 imagery card. Window widths should also be at least 10". The total of the two imagery paths is 20". That is, window size is 64 lines x 128 columns. During observations, first of all, adjusting telescope right ascension and declination coordinates makes celestial imagery enter into the window placed on the top of the screen. After it is appropriately placed, the base then stops rotating. After the center of gravity of images distinguished by computer are placed at suitable locations, number gathering begins. Windows follow celestial images as they shift downward, synchronously tracking. After completing the gathering of predetermined amounts of data, calculations are then carried out. From the beginning of collection to the presenting of results only requires 4 seconds. Utilization and operation of measurement instruments is very simple. Automation levels are very high.

#### 4 MEASUREMENT RESULTS

From November to December, 1992, we carried out measurements to be completed in 40 days at the Yunnan Observatory on Phoenix Hill in Kunming. This observatory is located 25°N at 2000m above sea level. Due to the fact that the weather is sometimes rainy or cloudy, only 20 segments of useful data were acquired. The time period for each iteration of observation was between 18:40 - 24:00. Through analysis of measurement results, it was discovered that the average value of  $r_0$  is 12.4cm (Unitized to the zenith location. The same below.). The range of changes was 2-28cm. The average value associated with  $\Theta_0$  is 10.6  $\mu$ rad. The range of changes is 3-27  $\mu$ rad. Fig.2 and Fig.3 are, respectively, observation results for  $r_0$  and  $\Theta_0$  on the two days, 4 and 5 December. From these Fig.'s, it is possible to see that changes associated with  $r_0$  are relatively smooth. However,  $\Theta_0$  changes are still relatively large. This clearly shows that changes associated with low atmosphere turbulence are not large. However, atmospheric turbulence flows associated with relatively high layers ( $h > 3 - 5$  km) are very unstable. Looking at this overall, the atmospheric seeing for Kunming in this period was very good. It can be compared to excellent observatory sites on a world scale, such as the U.S. Mauna Kea and Chile's La Silla.

During periods when use was made of coherence length and isoplanatic angle measurement instruments to carry out

observations of  $r_0$  and  $\theta_0$ , Zeng Zongyong and others fired temperature fluctuation space probe instruments at the same time to carry out measurements of  $C_s^2$ . Fig.4 is an actual example measured at 23:00 on 29 November 1993. In the Fig., curve b is the Hufnagel model [9]. Curve c is given by equation (3). In this,  $C_0 = 3.5 \times 10^{-14}$ .  $H_0 = 5400\text{m}$ . Their standard deviations relative to experimentally measured data are, respectively, 4.6 and 0.026. Coefficients of correlation are, respectively, 0.70 and 0.73. From this, it is possible to know that I models agree relatively well.

We made use of  $C_s^2$  probe data and  $r_0$  and  $\theta_0$  observation data for the same periods to carry out comparisons. In accordance with equation (2) and equation (8), respectively, calculations were gotten of  $r_0 = 14.4\text{cm}$  and  $\theta_0 = 8.3\text{\mu rad}$ . These two are in basic agreement. However, there are some relatively small differences. The causes for the differences that exist will be discussed in the sections that follow.

/219

Fig.2

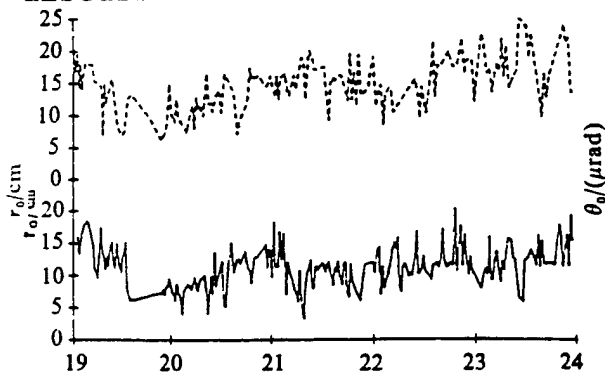


Fig.3

Beijing time/h  
Fig.2 The atmospheric coherence length vs time  
— : 1993. 12. 4 - - - : 1993. 12. 5

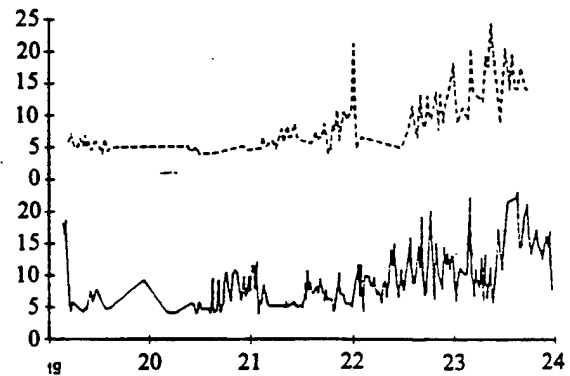


Fig.4

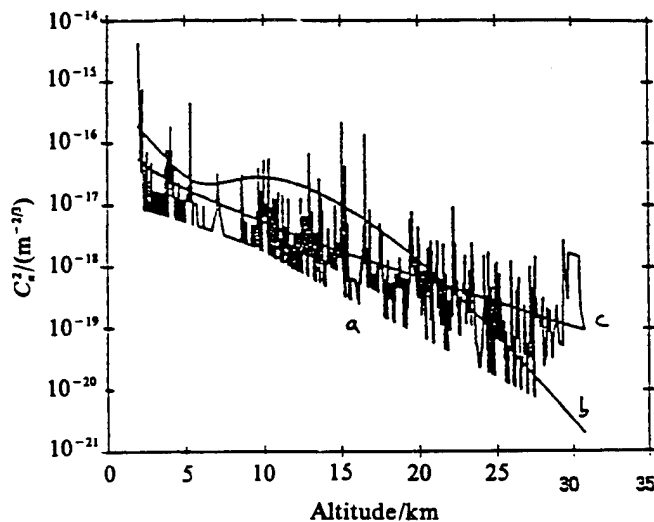


Fig.4 An example of measured  $C_s^2$  (23:00, Nov.29, 1993)

a. measured data; b. Hufnagel's model; c. Eq. (3)

## 5 CONCLUSIONS

The fact that there exist differences associated with measurement values and theoretical calculation values is also seen in the work of other scholars. For instance, Sydney and others [10] discovered  $r_0$  observed values to be 4.4cm. However, calculated values were 3.35cm. The two differed by 24%. The differences associated with  $\theta_0$  were even larger. This is entirely consistent with our results. In fact, it is reasonable that certain differences should exist. The reason is the measurement instruments themselves. No matter whether it is measurements of  $r_0$  and  $\theta_0$  or measurements of such parameters as  $C_n^2$ , there always exists a certain measurement error. As random quantity statistics, differences of around 20% are quite small. At the same time, theoretically, it is also possible for certain flaws to exist.

Speaking in terms of measurements, our imagery gathering speeds are not high enough. Sampling times are not long enough. This then creates frequency spectra in signals not being capable of complete coverage. Seen on the basis of frequency spectrum fluctuations, high frequency components ( $f \geq 10\text{Hz}$ ) are already extremely weak. Very large errors are not necessarily created. However, paying inadequate attention to low frequency components ( $f \leq 0.2\text{Hz}$ ) will give rise to relatively large errors. As a result, sampling times should be increased later. Secondarily, there is only a 15cm distance between the centers of the two telescopes associated with measuring instruments. It may be somewhat smaller. On the basis of Roddier's opinions, when  $d/D \geq 2$ , the accuracy of formula (7) is somewhat higher. However, this is not important. The shortening of interval distances will, no doubt, influence low frequency components. However, on the basis of the Taylor principles of frozen turbulence flows, if option is made for the use of multistage averaging, it will reduce in the same way the effects of low frequency components. One possible cause for the existence of relatively large differences in isoplanatic angles is that, according to theory,  $D$  should be 11cm. However, what we actually used was 12cm. Due to relatively large apertures possessing relatively large aperture smoothing effects, this leads to signal fluctuations becoming relatively weak. Thus, relatively large isoplanatic angles are obtained. Another possible cause which is more important is that, when solving formulae (2) and (8), consideration was not given to the influences of turbulent flow outside scales. As far as problems in this area are concerned, we have already made detailed analyses [11] in another report. It is not necessary to repeat them here. We only wish to point out this. After considering finite outside scales, based on a certain outside scale height distribution model, it is possible--with regard to the turbulent flow data discussed above--to do calculations and obtain  $r_0 = 20.9\text{cm}$  and  $\theta_0 = 12 \mu\text{rad}$ . These numerical values and

observed values are then in quite good agreement.

In summary, we are able to reach the following conclusions. Results obtained from coherence length and isoplanatic angle measurement instruments are reliable. After making certain improvements, it will then be possible to obtain even higher accuracies.

Acknowledgements Comrades Yan Peiying, Li Yanying, and others of the Academy of Sciences Photoelectric Institute participated in the development of the photomechanical parts of measurement instruments. During Kunming measurement periods, strong support was received from Comrades Wang Hanping and Leng Shengquan. For this, we all express our thanks.

#### REFERENCES

- 1 Fride DL, *J Opt Soc Am*.1966, **56**: 1372 ~ 1379
- 2 宋正方.四川激光.1984, **4**: 209 ~ 231
- 3 Barletti R et al. *Appl Opt*.1977, **16**: 2419 ~ 2421
- 4 宋正方.红外研究, 1982, **1**: 265 ~ 270
- 5 Moroder R and Righini A. *Astron & Astrophys*, 1977, **23**: 307 ~ 310
- 6 Roddier F. *In Progress in OPTics (ed E Wolf)*. 1981, **19**: 281 ~ 376
- 7 Loos G C and Hogge C B. *Appl Opt*, 1979, **18**: 2654 ~ 2661
- 8 Eaton F D, Peterson W A, Hines J R, and Fernandez G. *Appl Opt*, 1985, **24**: 3264 ~ 3273
- 9 Hufnagel R E. Dig of Tech Papers, Topical Meeting on Optical Propagation through Turbulence. Optical Society of American, Washington, 1974
- 10 Sydney P F et al. *SPIE* 1991, **1482**: 196 ~ 208
- 11 宋正方, 范承玉.湍流外尺度对大气相干长度和等晕角的影响(待发表)

A NEW APPROACH TO LASER CONDITIONING TECHNOLOGIES AND  
MECHANISMS ASSOCIATED WITH RAISING HIGH POWER LASER REFLECTOR  
MIRROR COATING DAMAGE THRESHOLD VALUES

Wang Yongzhong Zhang Yundong Xiang Shengming

Translation of "Ti Gao Qiang Ji Guang Fan She Jing Du Mo Sun  
Shang Yu Zhi De Ji Guang Hou Chu Li Ji Shu Ji Ji Li Tan Tao";  
HIGH POWER LASER AND PARTICLE BEAMS, Vol.6, No.2, May 1994, pp  
297-302

**ABSTRACT** This article introduces a type of laser conditioning technology associated with raising high power laser reflector mirror coating damage threshold values. In conjunction with this, it stresses using experimental and theoretical research on the mechanisms of raising laser damage threshold values to draw conclusions and make inquiries.

**KEY WORDS** Optical coating    Laser damage    Laser conditioning    Mechanism

## I INTRODUCTION

Following along with the wide spread application of high power lasers in fields such as tactical laser weapons as well as laser thermonuclear fusion, and so on, research associated with optically coated reflector mirrors possessing high laser damage threshold values has received more and more serious attention from people. The reason is that laser damage threshold values associated with optical coatings limit laser output powers. In the last more than ten years, a new type of technology has been developed--laser conditioning technology. It is capable of making laser damage threshold values associated with certain highly reflective mirrors go up two to three fold. Inside China and abroad, a number of hypotheses have been put forward in order to explain this phenomenon. What is regretable is that there is still not one type of theory capable of completely explaining it.

## 2 CHARACTERISTICS OF LASER CONDITIONING

### 2.1 Laser Conditioning Technology

As far as laser conditioning is concerned, it refers to a new technology which is capable of raising 2-3 fold laser damage threshold values after taking optical coatings or large pieces of optical materials and putting them through laser irradiation lower than laser damage threshold values. There are two types of laser irradiation methods associated with laser conditioning. One is using multiple iterations of laser irradiation of the same strength (s-on-1). Another type is using multiple iterations of laser irradiation with optical strengths which gradually go up over time (r-on-1). Using HfO<sub>2</sub>/SiO<sub>2</sub> and ZrO<sub>2</sub>/SiO<sub>2</sub> reflective film systems as examples, laser damage threshold values before laser conditioning are 7.4J/cm<sup>2</sup> and 7.1J/cm<sup>2</sup>. Going through laser conditioning, they rise respectively to 19.8J/cm<sup>2</sup> and 18.8J/cm<sup>2</sup>. Moreover, the latter type of laser conditioning method raises laser damage threshold values somewhat higher.

### 2.2 Relationships to Laser Parameters

Laser system parameters are different. Not only are damage threshold values different, but damage mechanisms also differ. Relationships between damage threshold values and wave lengths have roughly the relationship  $D_{\pm} \propto \lambda^x$ .  $x$  is a coefficient which changes along with film properties. The longer laser wave lengths are, the higher damage threshold values then are. The relationship between damage threshold values and pulse widths is  $D_{\pm} \propto \tau^{0.35}$ . When pulse widths are long, damage is primarily caused by absorption of focused heat. When laser pulses are short, dielectric breakdown created by electric fields is the primary factor in damage. Besides this, there are also relationships to such things as repetition frequencies of lasers, modes, and so on. Due to the fact that the relationships of laser damage threshold values and widths to wave lengths are the same before and after laser conditioning, as a result, damage mechanisms should also be the same before and after laser conditioning. This article limits itself to neodymium glass

laser spectral lines associated with irradiation laser light of 1.06 microns. Pulse widths are a few nanoseconds.

### 2.3 Relationships to Methods of Coating

Three types of methods are used to carry out tests: (1) commonly used electron beam evaporation; (2) ion beam spattering (IBS); and, (3) plasma plating (PP). Making use /298 of the latter two types of methods, the plated coating apertures are few (densities are high). Mechanical properties and environmental characteristics are good. However, experiments clearly show that their laser damage threshold values are still lower than films associated with electron beam evaporation. As far as carrying out laser conditioning on them is concerned, PP film laser damage threshold values are not raised much. Moreover, IBS laser conditioning is not necessarily effective. Generally speaking, laser conditioning is only effective with regard to electron beam evaporation coatings.

### 2.4 Relationships with Thin Film Materials

Thin film materials associated with high reflection mirrors in the visible and near infrared often use pairs of HfO<sub>2</sub>/SiO<sub>2</sub>, TiO<sub>2</sub>/SiO<sub>2</sub>, and ZrO<sub>2</sub>/SiO<sub>2</sub> to form reflection film systems. Because, after TiO<sub>2</sub>/SiO<sub>2</sub> plating, there is a requirement for drying in oxygen in order to reach complete oxydation so as to reduce absorption, this is not appropriate for reflection mirrors with large apertures. Besides that, in plating processes, TiO<sub>2</sub>/SiO<sub>2</sub> reflection mirrors cannot avoid producing intense absorption of low valance oxides of titanium. As a result, we only select ZrO<sub>2</sub>/SiO<sub>2</sub> and HfO<sub>2</sub>/SiO<sub>2</sub>. Making use of laser conditioning associated with pulse widths of 1ns, laser damage threshold values associated with the latter two are all raised roughly 3 fold. Replicability of laser damage threshold values associated with HfO<sub>2</sub>/SiO<sub>2</sub> is very good. Moreover, levels of increase with regard to various types of pulses are the same. Laser damage threshold values associated with ZrO<sub>2</sub>/SiO<sub>2</sub> follow along with different positions on reflector surfaces and change. Laser conditioning results are sometimes good and sometimes bad. However, making use of Nomarski microscopic techniques for observations, the flaw densities for the two are the same.

### 2.5 Relationships with Coating System Designs

With regard to three types of samples--lambda/4 HfO<sub>2</sub>, rich SiO<sub>2</sub> samples (includes 13 layers of lambda/4 SiO<sub>2</sub> between 10nm HfO<sub>2</sub>), and rich HfO<sub>2</sub> samples (includes 17 layers of lambda/4 HfO<sub>2</sub> between 10nm SiO<sub>2</sub>)--after laser conditioning, laser damage threshold values all go up approximately 2 fold. Because of this, there is no relationship between conditioning results and relative thicknesses of film systems. However, there is a type of exceptional special case. That is nothing else than that when the SiO<sub>2</sub> thickness is 0, that is, there is single layer HfO<sub>2</sub>, there are no conditioning effects.

### 3 INQUIRIES INTO LASER CONDITIONING MECHANISMS

#### 3.1 Early Explanations of Laser Conditioning

The first type of hypothesis is "laser cleanliness", that is, laser conditioning takes volatile impurities (in particular, water in the atmosphere) and gets rid of them from surfaces and the interior of coating materials. These impurities lead to laser damage. If this is the case, damage threshold value increases should be temporary. We took HfO<sub>2</sub> reflection mirrors which had not gone through laser conditioning and put them separately into environments at 20°C with relative humidities of approximately 50% for a period of time. Laser damage threshold values of 1064nm are measured. After that, use is then made of anhydrous P2O<sub>5</sub> and measurements are made again in 10 weeks. Observations are done of the shortening of wave lengths after the removal of water. It was discovered that, comparing laser damage threshold values before and after the removal of water, there were no alterations at all. However, reflectivity drift is reversible. The explanation of this is that laser damage threshold value changes are permanent.

Another type of hypothesis is that lasers take materials and heat them right up until their crystalinities change. In order to check this hypothesis, use was made of TEM and X ray diffraction in order to determine crystal structures associated with single and multiple layer films of HfO<sub>2</sub> and SiO<sub>2</sub>. Results clearly showed that SiO<sub>2</sub> in single and multiple layer films of 1 micron and 266 nm was no different at all. In all cases, it was in amorphous states. In contrast to that, HfO<sub>2</sub> crystal structures were related to thickness--smaller than 20nm, states were indefinite. As growth continued, by contrast, they were cylindrical crystals. They were primarily monoclinic crystals. Small numbers of cubes were also included. However, changes in relative thickness certainly did not influence conditioning effects. As a result, there was no relationship between laser conditioning and crystal structures. Making use of diffraction meters to carry out scanning with regard to thin films before and after laser conditioning, no differences were discovered.

#### 3.2 Electron Defect Model

Research personnel of the Lawrence Livermore National Laboratories (LLNL) put forward the existence [1] of a relationship between laser conditioning and electron defects inherent in films. Because electron beam evaporation processes are high speed quenching from high temperature steam to low temperature substrate, as a result, a porous film is produced with defects in its interior. There is a relationship between nonequilibrium states and laser conditioning characteristics. They believe that laser damage associated with thin films goes through the four steps below:

- (1) lasers take valence carrying electrons from restricted zones and excite them into conducting zones;
- (2) through photoelectric field or free current carrying particle absorption effects, free current carrying particles are

stimulated to achieve high energies;

(3) through ionization avalanche or photoelectric effects (crystal lattice heating), excessive amounts of energy are transmitted into crystal lattices; /299

(4) film materials are heated to critical damage temperatures--for instance, media material melting points.

The occurrence of laser conditioning phenomena is due to the elimination of the sources of conducting zone electrons in the first step, that is, as far as media material are concerned, under low flux laser irradiation, electrons in defects are excited into conduction zones. However, at this time, photoelectric fields are still not adequate to give rise to damage (steps 2-4). Electrons then decay into relatively deep energy levels. After that, it is not easy for them to be stimulated into conduction zones. When laser conditioning media make use of laser light below laser damage threshold values for irradiation, the number of electrons it is possible to use in order to transfer to conduction zones is already very small. As a result, the amounts of net energy transmited to crystal lattices is also small and does not go so far as to cause damage. In this way, conditioning effects are then produced.

Above is the basic thinking associated with the model in question. However, LLNL personnel also discovered a few experiments [2] that do not agree with the results that this model predicts.

Using ND.YAG lasers with wave lengths of 1064nm, 532nm, 355nm, and pulse widths of 10ns, respectively, to carry out laser conditioning with regard to 1 micron thick SiO<sub>2</sub> and HfO<sub>2</sub> single layer and multiple layer films, it was discovered that, in three wave lengths, SiO<sub>2</sub> single layers increased roughly 2 fold in all cases. However, HfO<sub>2</sub> single layer film laser damage threshold values still showed no increase at all. At the same time, LLNL personnel determined 1.06 micron,  $\lambda/4$  single layer HfO<sub>2</sub> and SiO<sub>2</sub> films. In them, HfO<sub>2</sub> films and 1 micron thick ones are the same. There are still no conditioning effects. However, the levels of increase associated with SiO<sub>2</sub> laser conditioning laser damage threshold values are still not higher than 30%.

If, with respect to laser damage threshold value  $D_T \propto \lambda^x$ ,  $x = \text{approximately } 1.0 \text{ for SiO}_2 \text{ single films and } x = \text{approximately } 1.9 \text{ for HfO}_2$ , laser damage threshold values are intensely influenced by wave length. In another area, damage forms are different. SiO<sub>2</sub> damage is a few small points (smaller than 5 microns), and they do not get any bigger with continued laser irradiation. Yet typical HfO<sub>2</sub> damage has diameters of 0.1-1 mm. This clearly shows that the methods of laser coupling to HfO<sub>2</sub> and coupling to SiO<sub>2</sub> are different.

With regard to multiple layer HfO<sub>2</sub>/SiO<sub>2</sub> films, after 1064nm laser conditioning, laser damage threshold values increase 2 fold. 355nm only have 40%. 533nm is then between the two. Laser damage threshold values at 1064nm are controlled by SiO<sub>2</sub>. However, at very short wave lengths, by contrast, the control is by HfO<sub>2</sub>. Due to HfO<sub>2</sub> absorption fringes associated with electron

beam evaporation at around 375nm, narrow band linear absorption inside HfO<sub>2</sub> may possibly be the cause controlling 355nm multiple film layer laser damage threshold values.

As a result, it is certainly not a single electron defect inside HfO<sub>2</sub> or SiO<sub>2</sub> which is then capable of determining conditioning effects. In that case, are electron defect models right in the final analysis or not? Up to now it has still not been possible to reach a conclusion. Perhaps a part of them is correct.

### 3.3 Recent Progress

Edwards and others carried out analyses [3] with regard to 1m ZrO<sub>2</sub>/SiO<sub>2</sub> Nova laser reflection mirrors plated by LLNL (The surface of the mirrors in question is unusually smooth. Roughnesses are 2.5-5nm). They discovered that the production of damage is begun from microscopic defects with diameters of approximately 30 microns. These defects form damage of approximately 250 microns, sometimes covering over 20% of the mirror surface. These defects lie inside thin films. In conjunction with this, they are of a two dimensional "disc" type. What is peculiar is that the damaged film surface is enveloped by a layer of "fog". They extracted these "fog" granules and discovered that they were precisely ZrO<sub>2</sub> and SiO<sub>2</sub> film materials. The explanation for this lies in material being splattered out in the damage process. In conjunction with this, it piles up on the film surface. Making use of SEM to observe these granules, diameters did not reach 1 micron. There was both surface smoothness and surface roughness. The former may possibly be formed from gas states condensing. However, the latter may possibly be solid state remnants thrown out.

Edward's explanation is that it is due to the defects in ZrO<sub>2</sub> material being heated, after laser irradiation, to temperatures sufficient to make the surrounding ZrO<sub>2</sub> gasify, that is, in excess of 3000K. In reference [4], Chase confirms that the cause which leads to this process is linear absorption. Is this type of so called defect a pure substance granule or not? Schildbach made use of laser mass analysis systems (LIMA), and, in conjunction with this, discovered no impurities at all [5]. In another area, due to defect densities being on the order of 100mm<sup>-2</sup> (with regard to the Nova reflection mirror), it is only when a vacuum chamber is severely polluted that it is possible to create this kind of outcome. In that case, may they not be low valence oxide materials--for instance, SiO<sub>2</sub>? Due to the fact that the Nova mirror laser damage threshold value is 7.8J/cm<sup>2</sup>, in this way, absorption coefficients associated with low valence oxides should be greater than 1000cm<sup>-1</sup>. Unfortunately, SiO<sub>2</sub> absorption coefficients (1 micron) still do not reach 100cm<sup>-1</sup>. What defects in SiO<sub>2</sub> are in the final analysis remains a puzzle even now.

/300

With regard to HfO<sub>2</sub> films, LLNL personnel, when studying electron paramagnetic defects, discovered that, contained in rich HfO<sub>2</sub> samples, there were special signals which were not in other samples. This type of signal clearly shows that HfO<sub>2</sub> may contain

in it Fe<sup>3+</sup> impurities (Commercially used HfO<sub>2</sub> film materials contain less than 0.05% Fe). This cannot be eliminated under laser irradiation below damage threshold values, leading to there being no conditioning effects.

Schildbach discovered that, when laser irradiation lower than the laser damage threshold (16-18J/cm<sup>2</sup>) is used on HfO<sub>2</sub>/SiO<sub>2</sub> reflective films, there are neutral particles of Hf, Si, and oxygen (including O and O<sub>2</sub>) sent out [5]. During initial emission, laser optical strength is 10J/cm<sup>2</sup>. Moreover, the critical optical strength required for conditioning is also just 10J/cm<sup>2</sup>. As a result, the emission of neutral particles is very possibly produced by laser conditioning. Neutral particle kinetic energies reach as high as a few score eV. High energy neutral particle emission corresponds to heat induced fractomission. Even if there is no obvious damage, this may still be the source of neutral particles. After heating of thin film defects, heat induced cracking is produced, leading to the elimination of absorbed material or the improvement of thermal stress fields (These are all causes giving rise to damage).

At the same time, Schildbach analyzed 8 points at different locations on mirror surfaces. He discovered that the conditioning results associated with them were certainly not the same. With regard to the 2 points which had not gone through processing, laser damage threshold values were 18-20J/cm<sup>2</sup>-- approaching laser damage threshold values associated with other points after processing. He believed that the cause for this was due to these two points not having any defects.

Staggs and others used atomic force microscopes (AFM) to observe reflection mirrors after plating. They discovered that most SiO<sub>2</sub> surfaces contain small mounds 200nm wide and 10nm high [6]. Moreover, HfO<sub>2</sub>/SiO<sub>2</sub> reflective film build ups are primarily irregular and are shallow pits or cores. Longitudinal dimensions are 1-10 microns. Transverse dimensions are approximately 1/3 of longitudinal dimensions. Densities are on the order of 10mm<sup>-2</sup>. After damage, the largest changes are the emission of cores. A round tunnel remains. Staggs paid attention to their being cracking on the edges of the tunnels. The cores are very sensitive to damage. When cores grow on thin films, due to shadow effects, moreover, the peripheries of cores are made to produce gaps, and they become flexible. Another characteristic of damage is the enlargement around 8 fold of small mounds in areas without defects in SiO<sub>2</sub> surfaces, that is, their growth or agglomeration. This type of surface agglomeration temperature is high enough to reach an ability to make components transition within time periods on the order of nanoseconds, causing the production of structures with large volumes and small surface areas. Structures clearly show that emission of cores occurs when using laser irradiation lower than laser optical strengths associated with making small mounds agglomerate.

Staggs carried out irradiation on defect areas. During the process of optical strengths increasing from 7.8J/cm<sup>2</sup> to 54.6J/cm<sup>2</sup>, AFM was used to analyze the appearance of defects.

There were still no obvious changes to the original outlines. However, after increasing to 19.8J/cm<sup>2</sup>, most 10nmx100nm cores disappeared from surfaces. After increases continued to 54.6J/cm<sup>2</sup>, there were no further changes. That is nothing else than to say that, as far as the production of surface smoothness phenomena in optical strengths emitted by cores is concerned, even though optical strengths continue to increase--exceeding laser damage threshold values--at the locations associated with these cores, still no damage occurred.

#### 4. CONCLUSIONS

To summarize what was discussed above, reflection mirror thin film damage is capable of definitely not resembling that type of complete cause in microscopic nonstable states considered by electron defect models, and, at the same time, is also not capable of being explained in all phenomena from a macro viewpoint. Combining electron defect models, we believe that the damage may go through the several steps below:

(1) Defects Inside Thin Films--Under Laser Irradiation--  
Stimulate the Production of Large Amounts of Free Electrons

Method A: Electron Ionization Avalanche

If free electrons which have broken out of their bonding already exist inside thin films, after laser irradiation, they go through electron ionization avalanche and form plasma bodies. The avalanche speed is represented as

$$\frac{dN_c}{d\tau} = \gamma(E) \times N_c$$

In the equation,  $\gamma(E)$  is ionization avalanche coefficient,  $N_c$  is conductance belt electron density, and  $E$  is field strength.

After that, energy absorption proceeded. Assuming that  $\eta(\xi, \tau)$  is the number of electrons with energies between  $\xi + \delta\xi$ . It is expressed as

$$\eta(\xi, \tau) = \eta(\xi) \exp(\xi \times \tau)$$

/301

Moreover, electron flux through isoenergetic planes is

$$J(\xi, \tau) = v(\xi) \times \eta(\xi, \tau) - D(\xi) \times \delta\eta(\xi, \tau) / \delta\xi$$

In this,  $v(\xi)$  and  $D(\xi)$  are, respectively, effective speeds and coefficients of diffusion associated with electron flows. Then, the energy distribution equation is

$$\frac{dJ}{d\xi} = \gamma(E) \times \eta(\xi)$$

Attached boundary conditions are

$$\eta(E_g, \tau) = 0$$

$$J(0, \tau) = 2 \times J(E_g, \tau)$$

In equations,  $E_g$  is the electrical gap of materials.

Method B: Going Through Valence Electron Transitions Given Rise to by Multiple Photons

At this time, the free electron densities produced by

stimulated valence electron transitions are

$$\frac{dN_c}{d\tau} = N \times \sigma^m \times F^m$$

In the equation,  $N$  is particle density,  $\sigma^m$  is multiple photon absorption,  $F^m$  is incident photon flow density.

(2) Free Current Carrying Particle Absorbtion Inside Defects

If crystal lattice temperature is  $T$ . On the basis of Drude models

$$c\rho \frac{dT}{d\tau} = \frac{N_c e^2 \tau E^2}{m(1 + \tau^2 \omega^2)}$$

In the equation,  $c$  is specific heat,  $\rho$  is crystal density,  $\tau$  is photon and electron collision time (approximately on the order of  $10^{-16}$  s),  $E$  is electric field strengths (effective value),  $m$  is electron effective mass, and  $\omega$  is laser angular frequency.

Combining the energy distribution equations above, the carrying out of integration over the entire energy space give laser energy absorption as

$$c\rho \frac{dT}{d\tau} = \delta \left\{ \int_0^{+\infty} \xi \cdot \eta(\xi, \tau) d\xi \right\} / \delta \tau = 1.09 (m^* kT / 2\pi)^{1/2} \cdot \frac{N_c}{L_{ac} v_s} \cdot \left( \frac{eE\omega}{m^*} \right)^3$$

In the equation,  $L_{ac}$  is the average free travel associated with electron and photon collisions,  $v_s$  is vertical wave speed, and  $m^*$  is electron belt mass.

(3) After Heating, High Density Defects Produce Agglomeration. In Conjunction with This Cracks which Are Made to Cover Thin Films Lead to Damage.

Laser conditioning is then the production of cracking in thin films under low flux laser irradiation, and, in conjunction with that, the causing of neutral particle emission. The results lead to laser damage cores being ejected. Conditioning results depend only on defect properties. Moreover, there is no relationship to such factors as thin film density, layer number, and so on.

The significance of laser conditioning research lies not only in being able to make our advances and improvements in laser conditioning technology, which is not yet mature. It is also being able to make us advance our understanding of the basic nature of laser damage.

#### REFERENCES

- 1 Wolfe CR *et al. SPIE*, 1990, **1433** : 360
- 2 Kozlowski MR *et al. SPIE*, 1991, **1441** : 269
- 3 Edwards G *et al. SPIE*, 1990, **1438** : 278
- 4 Chase LL *et al. J Appl Phys*, 1992, **71**(3): 1024 ~ 1028
- 5 Schildbach M *et al. SPIE*, 1991, **1441** : 287
- 6 Staggs MC *et al. SPIE*, 1992, **1624** : 375
- 7 Jones SC *et al. Opt Eng*, 1989, **28** : 1039

DISTRIBUTION LIST

---

DISTRIBUTION DIRECT TO RECIPIENT

---

ORGANIZATION	MICROFICHE
B085 DIA/RTS-2FI	1
C509 BALLISTIC RES LAB	1
C510 R&T LABS/AVEADCOM	1
C513 ARRADCOM	1
C535 AVRADCOM/TSARCOM	1
C539 TRASANA	1
Q592 FSTC	4
Q619 MSIC REDSTONE	1
Q008 NTIC	1
Q043 AFMIC-IS	1
E404 AEDC/DOF	1
E410 AFDTC/IN	1
E429 SD/IND	1
P005 DOE/ISA/DDI	1
1051 AFIT/LDE	1
P090 NSA/CDB	1

Microfiche Nbr: FID95C000759  
NAIC-ID(RS)T-0509-95